Robust polarization twist by pairs of multilayers with tilted optical axes

Adilkhan Sarsen and Constantinos Valagiannopoulos*
Department of Physics, School of Science and Technology, Nazarbayev University, 53 Qabanbay Batyr Ave, Astana KZ-010000, Kazakhstan

(Received 5 October 2018; revised manuscript received 4 February 2019; published 6 March 2019)

Polarization of photonic beams makes a continuous information carrier and thus modifying it dramatically within a short distance is desirable for numerous optical devices. The easiest way to emulate anisotropy, which is a prerequisite for any polarization conversion, is utilizing thin slices of plasmonic multilayers, whose performance is limited by the inevitable losses. Such a difficulty gets overcome by using pairs of these slices in a bilayer configuration and optimizing the direction of their optical axes. In this sense, the losses are balanced by the interplay between fields in each slice and the overall interference scheme yields closer-to-desired transmissions. Several realistic designs giving effective polarization twists of substantial immunity to fabrication defects or misalignment in oscillation frequency and incidence angle, are obtained. These structures are both efficient and minimalistic; thus can be useful in many photonic systems requiring robust polarization engineering and compact packaging.

DOI: 10.1103/PhysRevB.99.115304

I. INTRODUCTION

Since electromagnetic waves are comprised of two simultaneously varying field vectors in space and time, the polarization which defines the direction of these vectors is a crucial feature that can work as continuous information container, encoder, and encryptor [1]. Therefore, combining this characteristic of the flowing fields with directionally biased configurations is important in producing novel designs for a large set of photonic devices and has inevitably attracted substantial attention [2]. In particular, numerous optical systems depend their functionality on the input polarization such as structures achieving symmetry breaking through meta-atoms for circular [3] or noncircular [4] polarized light. Furthermore, the sensitivity of matter when interacting with differently polarized waves has given rise to fascinating nanodesigns supporting tunable coupling of surface plasmon polaritons [5] or controllable filtering properties [6].

Converting such a significant feature as the polarization of the traveling fields within a thin volume without reflection or other power losses is a challenging objective and thus has been a topic of many impactful theoretical and experimental investigations. The most common approach is employing anisotropic metasurfaces made of particles with suitable polarizabilities to combine the components of the propagated wave in terms of magnitude and phase, while achieving almost perfect matching [7]. The role of such particles that emulate anisotropy can be played by twisted complementary split-ring resonators sitting on chiral slabs [8] or high-contrast dielectric elliptical nanoposts with spatially modulated eccentricities [9]. Polarization conversion is also achieved with the use of rod resonators arrays which additionally enable anomalous refraction [10] or miniaturized printed metallic elements whose profile is dictated by implementing genetic algorithms [11]. Moreover, satisfying results are obtained when employing simpler structures like sequential tailored sheets [12] or just stacked nanorod arrays with rotated principal axes [13]. Finally, anisotropy creating efficient polarization twists can occur in homogeneous media either via proper bias like in graphene monolayers [14] or as a built-in property like in two-dimensional black phosphorus [15].

In this work, we emulate the essential anisotropy by stacking periodically two different media and show that perfect polarization twist for normal incidence is feasible even when employing just a single crosscut from this stack. In particular, the condition for such a flawless outcome is the huge asymmetry between the developed modes occurring when effective permittivity along one direction becomes singular. This demand is, in turn, fulfilled only if one of the two used media is plasmonic and the other dielectric (without necessarily emulating hyperbolic dispersion), but both of them lossless. Indeed, the insertion of any moderate losses, which is inherent to all plasmonic materials, harms significantly the output of the device. For this reason, we consider a pair of these slabs in a bilayer, which is the simplest planar configuration that can support resonances giving various interesting effects (asymmetric forces [16], wide-angle absorption [17], unidirectional tunneling [18]). The two paired pieces of that effectively anisotropic medium are taken identical, while the tilts of their optical axis are optimized for a variety of metallic materials in the visible and at the THz regime. Surprisingly, bilayers incorporating graphene, which is well known for its plasmonic response in THz frequencies, fail to deliver efficient twists in this design due to the two-dimensional nature of the monolayers. In this way, we obtain designs utilizing actual media that demonstrate highly efficient polarization conversion which is, additionally, extremely robust with respect to configuration imperfections, axes misalignment, and incidence obliqueness. The reported bilayers are characterized by structural simplicity revealing the physical mechanisms that provide the polarization twist, while there are several physical

*konstantinos.valagiannopoulos@nu.edu.kz

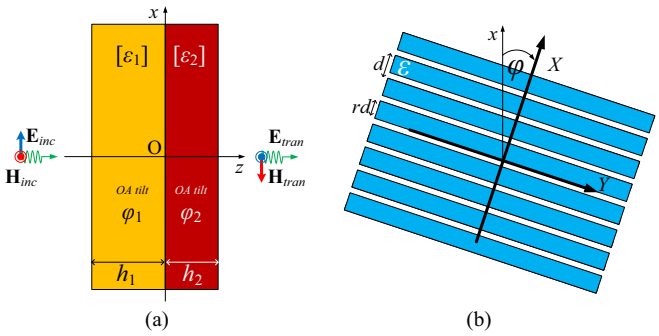

FIG. 1. (a) A pair of thin slabs with thicknesses (h_1, h_2) made of the same layered media with different optical axis (OA) tilts (φ_1, φ_2) serving as a perfect polarization converter for a normally incident plane wave. (b) Transverse view of the one of the slabs with optical axis tilted by angle φ: it comprises homogenized multilayers of plasmonic films (of permittivity ε) with airgaps in-between.

[19], chemical [20], and lithographic [21] deposition methods or even self-assembling approaches [22] to construct them. Therefore, we believe that our realistic structures may inspire the design of novel components processing the polarization of beams that demand substantial immunity to fabrication defects.

II. STRUCTURE AND TEXTURE

A. Effective permittivities

Consider the structure depicted in Fig. 1 where the used Cartesian coordinate system (x, y, z) is defined. Two thin planar slabs of thicknesses h_1 and h_2 are positioned back-to-back to form a bilayer being excited by a normally incident plane wave [Fig. 1(a)]. The texture of both slabs is identical and shown in Fig. 1(b): free-standing stack of films from the same (usually plasmonic) medium of relative complex permittivity ε with the same filling factor r and a spatial period d. However, the two slices are characterized by two different effective permittivity tensors $[\varepsilon_1]$ and $[\varepsilon_2]$ since the configurations are in-plane rotated (around the z axis) by different angles φ_1 and φ_2, respectively [defined like angle φ of Fig. 1(b)].

Let us denote as (X, Y, z) the local Cartesian coordinate system whose X axis is normal to the plasmonic/air interfaces in the multilayers constituting each slab. Under the assumption that d is optically small ($k_0 d \ll 1$, where $k_0 = 2\pi/\lambda_0$ is the free-space wave number and λ_0 is the operational wavelength into vacuum), the layered structure of Fig. 1(b) can be replaced by an effectively homogeneous uniaxial material with three permittivities $(\varepsilon_X, \varepsilon_Y, \varepsilon_z)$ along its major axes given by

$$\varepsilon_X = \frac{\varepsilon}{(1-r)\varepsilon + r}, \quad \varepsilon_Y = r\varepsilon + (1-r) = \varepsilon_z. \tag{1}$$

The expressions are obtained with the use of the static (homogenization, effective-medium) averaging approach [23]. Alternatively, one can use two-dimensional (2D) media instead of bulk plasmonic materials as shown in Fig. 1(b), which are characterized by complex surface conductivity σ (measured in Siemens) [24]. In such a case, the major effective permittivities of the multiple films are written as [25]

$$\varepsilon_X = 1, \quad \varepsilon_Y = 1 - i\frac{\sigma\eta_0}{k_0 d} = \varepsilon_z, \tag{2}$$

for suppressed harmonic time dependence $e^{+i\omega t}$, where $\omega = k_0 c$ is the oscillating frequency, c is the speed of light, and η_0 is the wave impedance into free space.

When one expresses these permittivities in the global Cartesian coordinate system (x, y, z), the tensors $[\varepsilon_1], [\varepsilon_2]$ take forms similar to

$$[\varepsilon] = \begin{bmatrix} \bar{\varepsilon} + \Delta\varepsilon\cos(2\varphi) & \Delta\varepsilon\sin(2\varphi) & 0 \\ \Delta\varepsilon\sin(2\varphi) & \bar{\varepsilon} - \Delta\varepsilon\cos(2\varphi) & 0 \\ 0 & 0 & \varepsilon_z \end{bmatrix}, \tag{3}$$

for $\varphi = \varphi_1, \varphi_2$, respectively, and $\bar{\varepsilon} = \frac{\varepsilon_X + \varepsilon_Y}{2}$ (average value), while $\Delta\varepsilon = \frac{\varepsilon_X - \varepsilon_Y}{2}$ (difference value).

B. Solutions and input/output parameters

The electric field vector of the incident field is selected to be parallel to x axis, namely it is written as $\mathbf{E}_{\text{inc}} = \hat{\mathbf{x}} e^{-ik_0 z}$ (with unitary amplitude 1 Volt/meter). Due to the anisotropy of the structure of Fig. 1, the reflected and the transmitted waves will have a nonzero y component and thus possess the expressions $\mathbf{E}_{\text{ref}} = (\hat{\mathbf{x}} R_x + \hat{\mathbf{y}} R_y) e^{ik_0 z}$ and $\mathbf{E}_{\text{tran}} = (\hat{\mathbf{x}} T_x + \hat{\mathbf{y}} T_y) e^{-ik_0 z}$, respectively. Our aim is to determine the conditions for the simple system of Fig. 1(a) to convert maximally the input field into a transmitted wave with polarization orthogonal to the former one (ideally $|T_y| = 1$ without reflections, for passive structures). Therefore, our metric measuring the success of this conversion would be the power carried by the y (cross-polarized) component of the electric field $P_{\text{cross}} = |T_y|^2$.

The propagation constants $\pm k_{\text{I,II}}$ of the waves developed longitudinally into a medium described by (3), characterized by the triplet of parameters $(\varepsilon_X, \varepsilon_Y, \varphi)$, are written as

$$k_{\text{I,II}} = k_0 \sqrt{\frac{(\varepsilon_X + \varepsilon_Y) \pm \sqrt{(\varepsilon_X - \varepsilon_Y)^2}}{2}}, \tag{4}$$

being independent from the tilt angle φ [and accordingly $\varepsilon_X, \varepsilon_Y$ are referring to the local Cartesian coordinate system (X, Y, z) given by (1) or (2)]. By imposing the necessary boundary conditions at $z = -h_1, 0, h_2$ one can readily find the reflection and transmission coefficients (R_x, R_y, T_x, T_y), whose explicit expressions are not shown for brevity. The following results have been validated by verifying the continuity of the tangential electric and magnetic components across the separating boundaries for every single of the investigated setups and designs.

III. NUMERICAL RESULTS

A. Ideal lossless media

Perfect polarization conversion can be achieved even for a single slice [like the one of the two of Fig. 1(a)] having the layered transverse structure of Fig. 1(b), as long as the utilized media are lossless. It is straightforward to find (from the analytic formulas of R_x and R_y) that the perfect matching

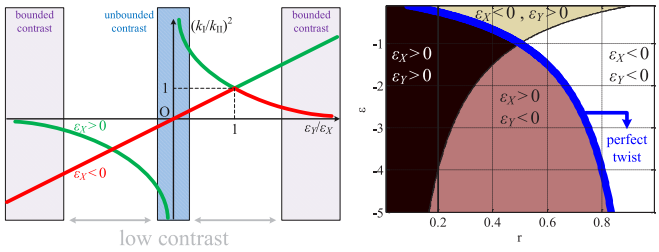

FIG. 2. (a) The squared ratio of the two supported modes $(k_I/k_{II})^2$ from (4), expressing the contrast between the two waves, as function of the (bounded) effective permittivity ratio $\varepsilon_Y/\varepsilon_X$ for positive (green) and negative (red) ε_X. The desired regime is shown in blue color (unbounded contrast). (b) The signs of the effective dielectric constants $(\varepsilon_X, \varepsilon_Y)$ from (2), on the plane of duty cycle r and plasmonic permittivity ε. The blue line corresponds to the blue region of Fig. 2(a) giving $\varepsilon_X \to +\infty$ and unbounded mode contrast; thus perfect polarization twist is achieved.

condition ($R_x = R_y = 0$) for a slab of thickness h reads

$$\sin(k_I h) = \sin(k_{II} h) = 0. \tag{5}$$

The thickness of the design should be kept electrically small ($k_0 h \ll 1$) as imposed by almost any practical, metasurface-type configuration; however, if both the arguments of sines in (5) are vanishing, we obtain just an infinitesimally thin ($h = 0$) and thus perfectly transparent ($T_x = 1$ and $T_y = 0$) film. On the contrary, 100% polarization conversion requires a dramatic change in transmission coefficients T_x, T_y which happens only when the sign of the corresponding cosines are different: $\cos(k_{I,II} h) = \mp 1$. Under the small-h assumption, this becomes feasible, in turn, only when the propagation constants $k_{I,II}$ differ considerably in magnitude, namely if $k_I \gg |k_{II}|$. Indeed, for a moderate (real or imaginary) k_{II}, we always obtain $\sin(k_{II} h) \to 0$ when $h \to 0$ and for a giant positive k_I, we can always find a small h at which $k_I h = \pi$. Such a demand reminds us clearly of the operation of the Fabry-Perot resonator; the polarization conversion effect is attributed to similar wave interference which guarantees perfect matching. However, conditions (5) should be combined with the aforementioned substantial modal contrast ($k_I \gg |k_{II}|$) which couples the two in-plane directions ($\varphi = 45^\circ$) leading to a perfect angular momentum twist.

To illustrate better the previous comments, in Fig 2(a), we show the (inevitably real) quantity $(k_I/k_{II})^2$ which indicates the contrast of modes as function of the ratio $\varepsilon_Y/\varepsilon_X$ of the effective permittivities along the major axes. One curve for $\varepsilon_X > 0$ (green) and another for $\varepsilon_X < 0$ (red) are sketched which, due to the form of (4), correspond also to the reverse contrast $(k_{II}/k_I)^2$ for the opposite selection of ε_X sign. The negative values of the green curve are owed to an evanescent mode of imaginary k_{II}, while the red curve sits below the horizontal axis when the wave with constant k_I is evanescent. Note also that, owing to the expression of (1), the ratio $\varepsilon_Y/\varepsilon_X$ can take a zero value (either $\varepsilon_Y = 0$ or singular ε_X for zero denominator) but never infinite values (ε_Y cannot be singular). Even approaching large magnitudes for ε_Y demands extremely dense dielectrics (with positive $\varepsilon \gg 1$), which are not easily found neither in visible nor at THz frequencies [26]. Therefore, despite that $k_I/k_{II} \to \infty$ for $\varepsilon_Y/\varepsilon_X \to \pm\infty$ as appears in Fig. 2(a), we cannot reach such points and thus the corresponding regions are labeled as of "bounded contrast" (since $\varepsilon_Y/\varepsilon_X$ is a bounded quantity). This is not the case when $\varepsilon_Y/\varepsilon_X \to 0$, which is the optimal regime and accordingly labeled as "unbounded contrast" region. For all the other values of $\varepsilon_Y/\varepsilon_X$, the contrast is low and the designs are of no interest.

Given the fact that $\varepsilon_Y = 0$ (ENZ behavior) usually leads to a balanced response between reflection and transmission [27], a single slab can work impeccably as angular momentum converter ($\varepsilon_Y/\varepsilon_X \to 0$) only for a large positive $\varepsilon_X \gg |\varepsilon_Y| \neq 0$ (and $\varphi = 45^\circ$). That outcome seems ruling out the use of 2D media in the described configuration for perfect polarization twist since, based on (2), ε_X is nonsingular and fixed; such a case will be further examined in the next subsection. Note finally that to make permittivity ε_X blow up (take singular values), one should work with $\varepsilon \cong -\frac{r}{1-r}$, which corresponds to a plasmonic and lossless material. Stacks with similar characteristics are well known for supporting alternative interesting effects like negative refraction [28].

As far as the characterization of the effective medium with macroscopic permittivities $(\varepsilon_X, \varepsilon_Y)$ is concerned, we can notice by inspection of Fig. 2(a) that huge asymmetry of modes, securing conditions (5), occurs only for $\varepsilon_X > 0$ but for both signs of ε_Y. In other words, the used medium can be either epsilon-positive ($\varepsilon_X > 0$ and $\varepsilon_Y > 0$) or hyperbolic ($\varepsilon_X > 0$ and $\varepsilon_Y < 0$), leading to a perfect angular momentum transformation for both cases. Therefore, the reported flawless result is not necessarily attributed to the hyperbolic dispersion relation but to the singular ε_X (regardless of the sign of ε_Y). In Fig. 2(b), we identify the dispersion of the homogenized material on the plane of duty cycle r and metallic permittivity ε; in this way, four domains are formulated: two describing common dielectric ($\varepsilon_X > 0$ and $\varepsilon_Y > 0$) and fully plasmonic ($\varepsilon_X < 0$ and $\varepsilon_Y < 0$) behavior and two indicating hyperbolic macroscopic response ($\varepsilon_X > 0$ and $\varepsilon_Y < 0$ or, alternatively, $\varepsilon_X < 0$ and $\varepsilon_Y > 0$). The parameter combinations (r, ε), making ε_X increase unboundedly, lie along the blue line $\varepsilon = -\frac{r}{1-r}$ coinciding with the borders between two pairs of the aforementioned regions. More specifically, for $r < 1/2$, the desired regime exists between hyperbolic (with $\varepsilon_X < 0$) and dielectric ($\varepsilon_X, \varepsilon_Y > 0$) parametric domain and for $r > 1/2$ is found at the common points of the other hyperbolic (with $\varepsilon_Y < 0$) and the plasmonic ($\varepsilon_X, \varepsilon_Y < 0$) region. However, as implied in Fig. 2(a), the behavior of the system is not the same regardless of the parametric side we achieve singular ε_X; indeed, ε_X should possess huge positive values (and thus ε should be slightly smaller than the limiting value $\varepsilon = -\frac{r}{1-r}$). That is because a vastly plasmonic $\varepsilon_X \to -\infty$ will create evanescent waves unable to match with free space [$\sin(k_I h) \neq 0$]. Once again, we notice that the perfect polarization twist is not an effect observed exclusively in hyperbolic media; it may also occur in dielectrics for $\varepsilon_Y > 0$ and $\varepsilon_X \to +\infty$ [Fig. 2(a)], namely for $r < 1/2$ and ε infinitesimally less than that indicated by the blue bound in Fig. 2(b).

It should be, therefore, remarked that the mechanism for the reported perfect polarization conversion is not the same to those creating an identical outcome in hyperbolic media. There are numerous proposed configurations such as silver nanowires in a MgF_2 matrix [29], grounded golden nanorods

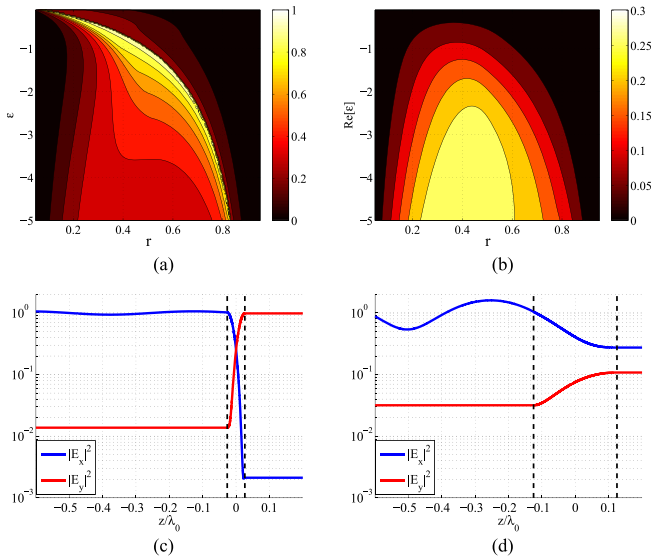

FIG. 3. (a) Maximum cross-polarization power output P_{cross} as a function of the portion of lossless plasmonic medium r and relative permittivity ε. (b) Same as Fig. 3(a) but the plasmonic medium is lossy with negative unitary imaginary part of permittivity. (c) Squared magnitudes of the two electric components $|E_x|^2$, $|E_y|^2$ as functions of the electrical distance z/λ_0 for the optimal lossless design of Fig. 3(a) with $\varepsilon \cong -0.92$. (d) Same as Fig. 3(c) for an optimal lossy design (with $\text{Im}[\varepsilon] = -1$) of Fig. 3(b) with the same $\text{Re}[\varepsilon] \cong -0.92$. Vertical dashed lines denote the boundaries of the slabs.

[30], metal-backed multilayers [31], graphene strips or disks [32], and metamaterial waveguides [33] which manipulate the polarization of the incoming light based on their hyperbolic macroscopic properties. However, our approach differs since the essential condition of the asymmetry of modes is achieved through a resonant permittivity $\varepsilon_X \to +\infty$, without necessarily a negative $\varepsilon_Y < 0$ that makes a hyperbolic dispersion relation.

In Fig. 3(a), we represent the maximum transmitted power along the cross-polarization direction $\max_{\{0<\varphi<360^\circ,\, 0<h<0.25\lambda_0\}} P_{\text{cross}}$ by considering all possible optical axis rotations φ and a continuous range for electrical thicknesses less than a quarter of free-space wavelength: $0 < h/\lambda_0 < 0.25$. The quantity is represented in contour plot with respect to filling ratio r and the permittivity ε of the layered medium. We realize that 100% polarization conversion in the considered lossless design happens along (and slightly below) the line $\varepsilon = -\frac{r}{1-r}$ which makes an unbounded ε_X from (1), as mentioned above. It is noted again, as indicated by Fig. 2(b), that an ideal twist can be achieved either for a dielectric ($r < 1/2$) or for a hyperbolic ($r > 1/2$) homogenized medium. However, it is well-known that plasmonic response is always accompanied by inevitable losses ($\text{Im}[\varepsilon] \neq 0$). If one considers a moderate imaginary part for ε ($\text{Im}[\varepsilon] = -1$) and repeats the optimization of Fig. 3(a) on the (r, $\text{Re}[\varepsilon]$) map this time, one obtains Fig. 3(b). It is obvious that the maximal power for polarization twist does not surpass 30% and thus we have a clear indication that in the presence of realistic losses the effect gets substantially harmed, as commonly reported [34].

In Fig. 3(c), we show the spatial distribution of the two (squared magnitudes of) electric components $|E_x|^2$, $|E_y|^2$ as a function of z/λ_0 when a highly efficient polarization conversion is achieved according to the map of Fig. 3(a), namely for $\varepsilon \cong -0.92$ and $r \cong \frac{\varepsilon}{\varepsilon-1} = 0.48$ (ordinary epsilon-negative uniaxial dielectric in the absence of losses). We notice that for such a layered medium and $\varphi \cong 45^\circ$, we educe almost perfect result within an ultrashort distance ($h < 0.06\lambda_0$). The two components vary abruptly and linearly into the slab and negligible reflections are occurred; furthermore, the transmitted $|E_x|^2$ retaining the direction of the incident field is smaller than 0.2% of its power. On the contrary, in Fig. 3(d), where the best lossy scenario (with the same real part of permittivity) is considered, we remark significant reflections and a very poor polarization conversion; $|E_x|^2$ is almost triple the $|E_y|^2$ in the transmission region.

B. Actual lossy plasmonics

As shown in Figs. 3(b) and 3(d), losses constitute a bottleneck for the efficient polarization shift via a single slab and thus we cannot ignore them in our realistic examples. For this reason, we are considering the bilayer of Fig. 1(a) where the initial slab is split in two pieces that get in-plane rotated. Such a slight structural modification will not change the used media or their configuration at all, but will create a new pair of waves in each slab which will interfere each other to give a transmission with higher polarization conversion degree. To put it alternatively, we are using exactly the same lossy material and the same thin size in an identical multilayer setup; however, the result is expected to be much better due to the fields interplay emerging simply by rearranging the structure.

Given the fact that metals in the visible part of frequency spectrum exhibit plasmonic properties with relatively suppressed Ohmic effects, we are considering some of the most common and least lossy of them (aluminum, gold, silver). Their permittivity profiles $\varepsilon(\lambda_0)$ are obtained from the well-established material database [35] containing reliable experimental data from highly cited references [36]. In the following, we also assume that the dielectric permittivity ε of the materials remains the same at a specific wavelength λ_0, regardless of the sample thickness or their spatial neighborhood.

In Fig. 4(a), we perform a maximization of P_{cross} by keeping the thickness h of the slab fixed each time and additionally varying internally the duty cycle $0 < r < 1$ in a system that the role of plasmonic medium is played by aluminum for 400 nm $< \lambda_0 <$ 700 nm. Contrary to Fig. 3(b), where for every single point of the map we optimized (h, φ), in Fig. 4(a) we sweep the parametric ranges of (r, φ). Again, the final outcome is similar: the losses make the performance P_{cross} of our device not to surpass 30%. However, if one uses the bilayer structure of Fig. 1(a) instead of a single slab with the same overall thickness $h = h_1 + h_2$ and, most importantly, the same plasmonic characteristics (ε, r), the result gets substantially improved with no additional equipment (such as utilization of active media [37] or heavy doping processes [38]). Indeed, in Fig. 4(b), where we perform maximization with respect to three parameters: $(h_1, \varphi_1, \varphi_2)$ with

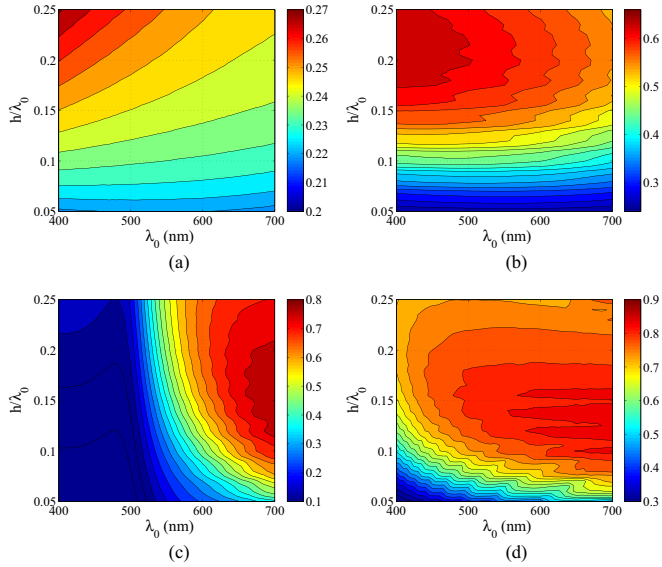

FIG. 4. Maximum cross-polarization power output P_{cross} as a function of the operational wavelength λ_0 (visible) and the electrical thickness of the structure $h/\lambda_0 = (h_1 + h_2)/\lambda_0$ for (a) aluminum-air slab, (b) aluminum-air bilayer, (c) gold-air bilayer, (d) silver-air bilayer.

$h_2 = h - h_1$ for every single point of the plane $(\lambda_0, h/\lambda_0)$, the total performance is increased more than two times. We note that the results in Figs. 4(a) and 4(b) are directly comparable to each other since the structure of Fig. 4(b) comes from the corresponding one of Fig. 4(a) by properly cutting the slab in two parts and suitably rotating their optical axes on xy plane. It is additionally clear that, unlike the single slice, the highest conversion does not happen for the thickest sample $(h_1 + h_2 = 0.25\lambda_0)$ but at a smaller h. As far as the operational frequency is concerned, in both designs (slab and bilayer), the aluminum-loaded configuration prefers the violet color.

In Fig. 4(c), we consider free-standing golden multilayers and repeat the same process as in Fig. 4(b) for the bilayer of Fig. 1(a). One notices that gold gives the best result for red color illumination (where $|\text{Im}[\varepsilon]|$ drops abruptly) and in that case the polarization conversion becomes as high as 80%. The findings are even more interesting in Fig. 4(d), where the utilized metal is silver (Ag): its deeply plasmonic response combined with inherent low losses, give performances P_{cross} up to 90% for $\lambda_0 > 550\,\text{nm}$ covering part of the green color spectrum and the entire ones for yellow, orange, and red. Notice that the occurred thickness resonances admit almost perfect conversion for very thin surfaces $(h = h_1 + h_2 < 0.1\lambda_0)$. It should be also emphasized that the optimization with respect to the tilts (φ_1, φ_2) as in Figs. 4(b), 4(c) and 4(d) is more effective than optimizing the bilayer for different duty cycles but the preselected arbitrary rotation of optical axes. Indeed, the parameters (φ_1, φ_2) offer more redundant degrees of freedom to system design without requiring modification of the structure. One should finally stress that the conditions for perfect polarization twist in the single lossless slab do not necessarily carry over to the examined lossy bilayer; the interplay between the developed waves can give high scores without demanding the use of plasmonic media.

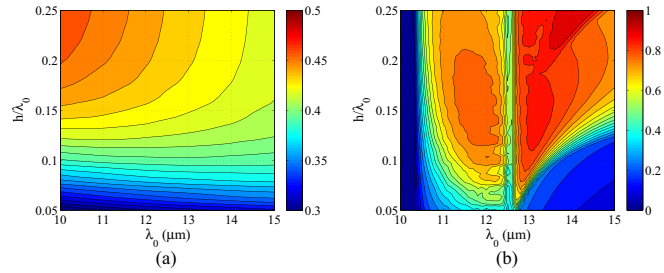

FIG. 5. Maximum cross-polarization power output P_{cross} as a function of the operational wavelength λ_0 (THz) and the electrical thickness of the structure $h/\lambda_0 = (h_1 + h_2)/\lambda_0$ for (a) graphene-air bilayer, (b) silicon carbide-air bilayer.

A famous material that exhibits negative effective permittivity combined with tiny Ohmic effects is two-dimensional graphene when working in the THz regime, which also possesses a number of other advantages (such as durability). Graphene conductivity σ is a sum of two terms: one corresponding to the transition of electrons within the same energy level (intraband transitions, low-energy plasmons, σ_{intra}) and another describing the hop of charges to neighboring energy levels (interband transitions, high-energy plasmons, σ_{inter}). The related formulas are extracted with use of the Kubo model [39] and give $\text{Im}[\sigma] < 0$ (plasmonic behavior) with suitable doping for the entire THz band. In Fig. 5(a), we perform maximization of P_{cross} for the structure of bilayer when each of the layers is comprised of periodic (with spatial period d) graphene nanoribbons [40]. The electron doping (chemical potential bias) and relaxation time (rate of energy conversion to Ohmic form) are selected with typical values and the graphene stack is quite densely populated to enhance the plasmonic response. The polarization transformation ratio is very low (below 50%) even though the bilayer configuration is utilized; such a finding, has been also obtained in the case of the single slab. That is because, according to (2), $\varepsilon_X = 1$ (equal to the host material, namely vacuum), since the 2D media cannot interact with electric fields normal to their surface. Therefore, the condition for unbounded ε_X (or ε_Y), which gives significant polarization tilt as previously discussed, cannot be fulfilled despite the plasmonic character of graphene. Indeed, only patches of graphene deposited normally to the direction propagation, on dielectric bases, have been reported to achieve cross-polarization transformation [40,41].

On the contrary, if one uses another bulk medium with similar features at the same frequencies, like silicon carbide (SiC), the results are much better. Across this wavelength range $(10\,\mu\text{m} < \lambda_0 < 15\,\mu\text{m})$, its permittivity follows a Lorentz dispersion model, according to which [42] $\varepsilon(\lambda_0) \cong 6.5(1 + \frac{\lambda_0^2}{2.07\lambda_0^2 + i0.09\lambda_0 - 326})$, where λ_0 is measured in μm. These very low losses make the maximal P_{cross} to have the variation of Fig. 5(b) on $(\lambda_0, h/\lambda_0)$ map for the case of two free-standing SiC multilayers. One directly notices that almost perfect polarization conversion is feasible for specific configurations operated at $\lambda_0 > 12.5\,\mu\text{m}$, while large scores are also recorded for $\lambda_0 < 12.5\,\mu\text{m}$. When $\lambda_0 \cong 12.5\,\mu\text{m}$, $\text{Re}[\varepsilon]$ of silicon carbide vanishes and we obtain a $P_{\text{cross}} \cong 50\%$ regardless of the selection of the rest of parameters, indicating the balanced response from ENZ media [27].

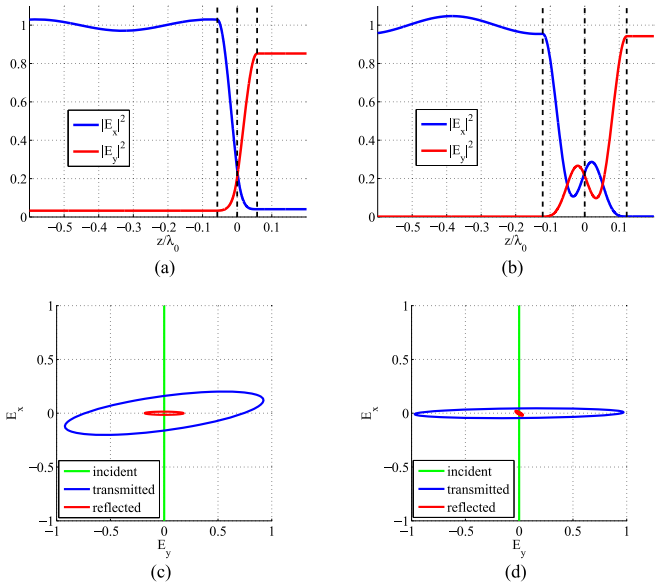

FIG. 6. (a,b) Squared magnitudes of the two electric components $|E_x|^2$, $|E_y|^2$ as functions of the electrical distance z/λ_0 for the optimal bilayers of (a) Fig. 4(d) with silver-air multilayers at $\lambda_0 = 700$ nm ($\varphi_1 \cong 12^\circ$, $\varphi_2 \cong 76^\circ$, $h_1 = h_2 \cong 0.058\lambda_0$, $\varepsilon \cong -23.7 - 0.534i$, $r \cong 0.87$) and (b) Fig. 5(b) with silicon carbide-air multilayers at $\lambda_0 = 14.1\,\mu$m ($\varphi_1 \cong 36^\circ$, $\varphi_2 \cong 55^\circ$, $h_1 = h_2 \cong 0.12\lambda_0$, $\varepsilon \cong 21.6 - 0.224i$, $r \cong 0.83$). (c,d) Patterns sketched by the tips of the electric field vectors of incident, transmitted, and reflected waves for (c) the case of Fig. 6(a) referring to the optimal of Fig. 4(d) and (d) the case of Fig. 6(b) referring to the optimal of Fig. 5(b).

Note that, as indicated by Figs. 4(b), 4(c) 4(d), and 5(b), there are numerous alternative designs which are working efficiently for various frequencies of the considered bands. These optimized setups, due to the careful and thorough sweeping of the parametric space, give performances that constitute limits for such a simplistic structure at the corresponding operational wavelength λ_0, as long as materials with realistic losses are employed. In other words, we show results which are not just the outcome of a tedious maximization of an objective function; in fact, they set bounds which cannot be surpassed without smarter structures (patterns of complex boundaries) or textures (artificial media and metasurfaces).

To demonstrate the efficient polarization conversion in realistic designs, we pick two of the most successful bilayers to observe the spatial distribution of the signals in Figs. 6. The first one [Ag-air multilayers, Fig. 6(a)] is operated at the visible red light $\lambda_0 = 700$ nm and the other [SiC-air multilayers, Fig. 6(b)] is working at $\lambda_0 = 14.1\,\mu$m. In the former case, we observe a linear variation of the signals $|E_x|^2$ and $|E_y|^2$ into the structure [similar to that of Fig. 3(c)], while very mild reflections are occurred, especially for the first quantity; furthermore, the wave with electric field parallel to the x axis that passes from the other side is of small power. The corresponding magnetic fields get maximized at the interface between the two media ($z = 0$) which is common in bilayer configurations [18]. In the latter case, the polarization conversion is very high, while the signals get locally maximized and minimized into the bilayer following opposite trends. The reflection for $|E_y|^2$ and the transmission for $|E_x|^2$ are practically absent, while only a weak reflecting oscillation is present for $|E_x|^2$.

In Figs. 6(c) and 6(d), with the observer located at a fixed xy intersecting plane being normal to the z direction of propagation, we show the shape described by the tip of the electric field vectors: incident (green), transmitted (blue), and reflected (red), as the time goes by. In Fig. 6(c), where the design of silver-air multilayers of Fig. 6(a) is considered, we notice that the ellipse of the transmitted wave is quite elongated and almost parallel to y axis; on the contrary, the magnitude of the reflected wave is much smaller and exactly oriented along y axis. In Fig. 6(d), where the design with silicon carbide-air multilayers of Fig. 6(b) is considered, we observe an almost perfect outcome with an extremely elongated polarization ellipse, practically on the y axis, for the transmitted wave and a negligible reflected field. By inspection of Figs. 6(c) and 6(d), one directly concludes that similar bilayer structures and the same optimization technique can be used for transforming the linear polarization of the incoming waves into circular or elliptical with certain eccentricity [15,41]. When it comes to our assumption for free-standing multilayers (background vacuum), which is adopted in all the presented numerical examples, it does not constitute a significant limitation; indeed, we have run the optimizations by considering a dispersionless dielectric instead of vacuum (teflon) and found similar results. In other words, the maximum polarization conversion is equally high (for a different optimal design) regardless of the transparent medium used to deposit metallic surfaces; such an outcome makes an advantage towards fabrication of the prototypes. It should be finally mentioned that, despite the elliptic polarization of the transmitted field produced by a linear plane wave, the overall angular momentum is conserved since the reflected ray bridges the difference.

Due to the reciprocity of the bilayer, the specific designs of Fig. 6 work almost perfectly for a y-polarized field traveling along the negative z axis from $z \to +\infty$. However, the device fails when one permutes the two layers even though their thicknesses are equal ($h_1 = h_2$) in both structures; in this way, the unilateral operation of the proposed structures is demonstrated. Furthermore, as an alternative to the configurations of Fig. 1(a), tested in Fig. 6, one can use metallic mirrors as substrates and check the cross-polarization response solely in reflection [11,41] given the fact that it is harder to achieve polarization conversion in transmission.

Regarding the actual construction of the aforementioned multilayers, there are several ways of fabricating them starting from the set of chemical techniques whose more representative member is the so-called atomic layer deposition (ALD). It is a sequential approach where reactive media are sprayed by other substances (precursors) enabling successive chemical reactions each of which generates a new layer [43]. Photonic multilayers of noble metals such as Ag is a common outcome of ALD [20], while stacks of SiC films have been built by using similar approaches [44,45]. Another fabrication category of planar multilayers consists the physical depositions and especially molecular beam epitaxy (MBE), where a heated substrate gets shot by guns of the successive media in gas form, molecule-by-molecule [19]. Again, stacks of metals in the visible and semi-conductors [46], like SiC, in the THz regime can be produced by such a technique. Moreover,

lithography may be employed successfully for manufacturing of gradient metasurfaces with rectangular rods which constitute the building block [Fig. 1(b)] of the reported designs [21]. Finally, similar lamellar structures can be even self-organized [22] by utilizing plasmonic eutectics in combination with suitable micropulling. In most of the aforementioned approaches, the deposition of layers with thickness much smaller than the oscillation wavelength λ_0 is possible and thus the homogenization assumption for $d \ll \lambda_0$ [with reference to Fig. 1(b)], yielding the approximate formulas (1), is realistic and justified. Therefore, the simulation of the stacked tilted layers forming each slab and examination of the Floquet-Bloch modes [25] excited into each slab followed by matching them across the boundaries $z = -h_1, 0, h_2$, is not necessary.

It should be mentioned that a rather challenging part in fabricating the structure of Fig. 1, is to extract two very thin multilayered structures [like that of Fig. 1(b)] and place them back-to-back in free space. A possible remedy to such a weak point is to grow the structure on a penetrable or transparent substrate; by modifying the used metrics and following exactly the same optimization scheme, the obtained result will be similar as long as the losses of the dielectric substrate are negligible and its thickness properly selected. However, even if one insists to build such a setup in vacuum background, there are lift-off techniques which have been implemented successfully in similar free-standing metasurface structures both in the visible spectrum [47] and especially at THz frequencies [48,49].

C. Robustness of performance

It would be meaningful to check the performance of the proposed bilayer designs when small changes in the structural and excitation parameters are occurred. Since the presented concept is based on the suitable rotation [50] of the optical axes to maximize the polarization conversion, it makes sense to start by examining the behavior of the device under imperfect tilts (φ_1, φ_2). In Fig. 7(a), we show the metric P_{cross} on the (φ_1, φ_2) plane within a range of $\pm 20^\circ$ around the central operation point (marked with black $\times$ sign), for the design with Ag-air multilayers of Fig. 6(a). We notice that the performance of the considered bilayer is insensitive to tilt errors of at least 5° for both angles, while its tolerance gets further increased in case the deviations of the two rotations are combined. In Fig. 7(b), the cross-polarization power output is represented on (φ_1, φ_2) map, similarly to Fig. 7(a), but for the SiC-air multilayers of Fig. 6(b). It is also clear that P_{cross} remains close to its maximal value even for more substantial errors of tilts (around 10°). Therefore, one can say that the presented bilayers do no require very careful construction in terms of rotation or, reversely thinking, that almost perfect polarization conversion can be achieved for waves with a wide range of electric-field directions (other than x) on the xy plane.

In Figs. 7(c) and 7(d), we represent again P_{cross} but with respect to imperfections of size; in particular, changes in h_1/λ_0 and h_2/λ_0 around the optimal choice are considered. The operational point is denoted again by a black $\times$ and the black dashed line corresponds to the ideal fixed overall thickness $h_1 + h_2 = h$. In Fig. 7(c), we examine the design of Ag-air multilayers of Fig. 6(a) and find that the cross-polarized power

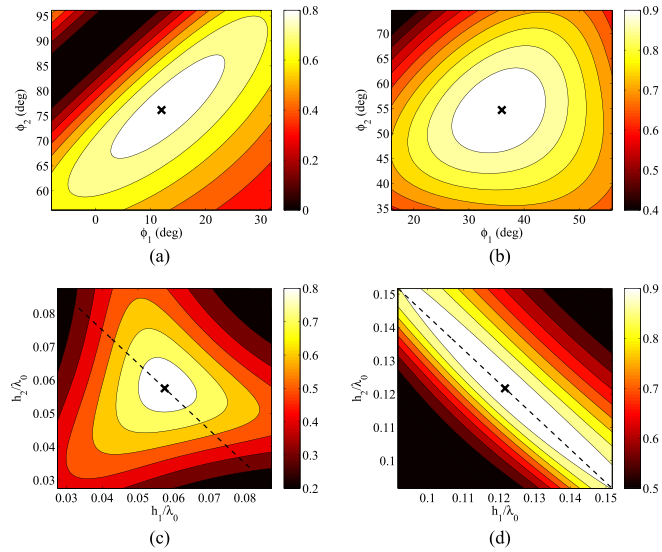

FIG. 7. Cross-polarization power output P_{cross} in a contour plot with respect to (a, b) the optical axis tilt angles (φ_1, φ_2) and (c, d) the electrical thicknesses of the two layers $(h_1/\lambda_0, h_2/\lambda_0)$. Two designs are examined (a, c) the Ag-air multilayers at $\lambda_0 = 700$ nm of Fig. 6(a) and (b, d) the SiC-air multilayers at $\lambda_0 = 14.1\,\mu$m of Fig. 6(b).

drops somehow abruptly with respect to both thicknesses. However, the deterioration of the performance is higher when both h_1 and h_2 are selected larger (than optimal) compared to the case that thinner slices are employed, despite the fact that we are referring to an already thin design. In Fig. 7(d), where the SiC-air multilayers of Fig. 6(b) are considered, we observed that imperfections in h_1 and h_2, play no role as long as the total thickness remains the same. Such a feature is due to the small difference between optimal angles as shown in Fig. 7(b), which is not the case for the other design [Fig. 7(a)]. Furthermore, the minimum recorded performance is higher than in the case of Ag-air multilayers for the same value range of h_1/λ_0 and h_2/λ_0 around the operational point, since SiC-air structure is optically thicker. Finally, and contrary to Fig. 7(c), the decrease in P_{cross} occurs in both ways: either we choose larger h_1, h_2 or smaller than the optimal. As a general conclusion, one may infer that the proposed constructions are retaining their polarization conversion capability, even when the thicknesses of two pieces are not very carefully controlled.

Another parameter related to fabrication of the films stacks of Fig. 1(b) is the duty cycle of the plasmonic material r

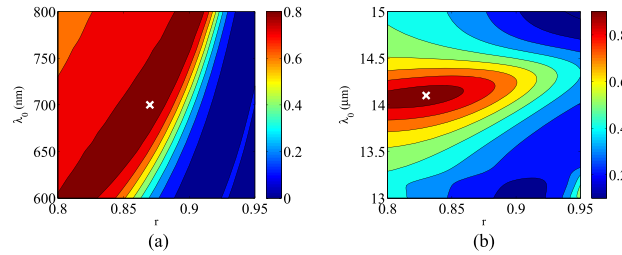

FIG. 8. Cross-polarization power output P_{cross} as a function of the plasmonic portion r and the operational wavelength λ_0 for (a) Ag-air bilayer (visible) of Fig. 6(a) and (b) SiC-air bilayer (THz regime) of Fig. 6(b).

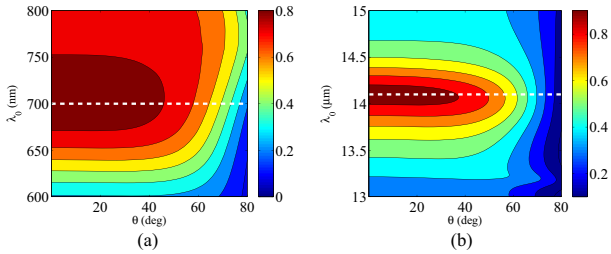

FIG. 9. Cross-polarization power output P_{cross} as function of the obliqueness angle θ and the operational wavelength λ_0 for (a) Ag-air bilayer (visible) of Fig. 6(a) and (b) SiC-air bilayer (THz regime) of Fig. 6(b). White dashed lines indicate the optimal wavelength.

and thus is necessary to examine the variation of P_{cross} under imperfect selection of this parameter. In Fig. 8, we show our metric in contour plot with respect to r and the working wavelength λ_0 (to investigate additionally the effect of the material dispersion on the output). Again the two designs of Fig. 6 are considered, while the operating point is denoted with a white $\times$ sign. We note that the performance of the first design [Fig. 8(a), Ag-air in the visible] drops abruptly for larger r but retains its high values when duty cycle is smaller. When it comes to its wideband features, P_{cross} exhibits substantial immunity to changes in λ_0, especially when it deviates towards the infrared part of the spectrum. In Fig. 8(b), where the THz-operated structure is considered, we remark that the sensitivity of the device with respect to r defects is similar regardless of the error sign (for less or more than the central value). However, the frequency response of the bilayer is sharper than that of Fig. 8(a), given the fact that the working bands are always a fraction of the central wavelength.

In all the previous analysis and examples, we assume normal incidence of the electromagnetic wave on the planar surface of the bilayer. Therefore, it is important to understand if the reported substantial polarization conversion is present when this significant assumption is not fulfilled. We solved the formulated boundary value problem for a wave with x-polarized electric field $\mathbf{E}_{\text{inc}}$ traveling along the direction forming an angle θ with the z axis and evaluated the corresponding cross-polarized power along the transmission direction: $P_{\text{cross}} = |T_y|^2 \sec^2\theta$. Note that the obtained variations are similar when assuming oblique incidence by keeping magnetic field $\mathbf{H}_{\text{inc}}$ parallel to y axis. The results are shown in Fig. 9 where the conversion metric is represented as function of the obliqueness angle θ and (again) the working wavelength λ_0; the ideal wavelength is indicated with a white dashed line. in Fig. 9(a), where the optimal Ag-air multilayers are once more examined, we realize that P_{cross} remains very high for a large band around the central wavelength $\lambda_0 = 700\,\text{nm}$ and simultaneously exhibits remarkable robustness with respect to angle θ: even for oblique incident rays of $\theta = 45^\circ$, the transformation rate retains its substantial magnitude ($P_{\text{cross}} \cong$ 80%). In Fig. 9(b) referring to SiC-air design, we have a similar wide-angle response accompanied by a more rapid drop of the performance if one deviates from the working frequency [as also indicated in Fig. 8(b)]. In both cases, however, considerable insensitivity with respect to the direction of incident beam is demonstrated, which permits the proposed design to operate for an extended cone of rays around the normal axis. Significant role towards the detection of such robust and efficient structures has been played by the thorough scanning of the parametric space and the careful optimization with respect to angles (φ_1, φ_2), duty cycle r, and optical thickness h/λ_0, executed in Sec. III B.

IV. CONCLUSION

Flawless polarization conversion can happen into thin slices of multilayers stacking periodically films of plasmonic media on dielectric ones, as long as the occurred losses are negligible. However, this condition cannot be fulfilled since metallic properties are always accompanied by inevitable Ohmic thermal conversion. As a remedy, one may use a pair from these slices, instead of an isolated one, and suitably rotate them resulting in significantly improved polarization twists, even in the presence of losses. We examine several plasmonic materials (including two-dimensional graphene) under variable frequency illumination and propose optimized efficient designs with increased immunity to structural imperfections, which additionally support wideband and wide-angle operation.

The introduced components are both conceptually simple since the bilayer is the minimal planar structure that can support a resonance, and realistic because various different fabrication methods are applicable. Accordingly, our approach can be utilized for multiple polarization-engineering objectives by optimizing more than two metallodielectric stacks and thus our designs can be used as building blocks of various novel photonic devices in the visible and at THz regime.

Finally, the findings of this paper suggest that analogous concepts can be carried over to quantum optics architectures for twisting and converting the spin or orbital angular momentum of light [51]. It is, therefore, expected that the utilization of various states of angular momentum for optical communications, working as different carriers for transmitting parallel data streams [52], will offer unprecedented capacity levels to the respective integrated systems.

ACKNOWLEDGMENTS

This work has been supported by Nazarbayev University Small Grant No. 090118FD5349 ("Super transmitters, radiators, and lenses via photonic synthetic matter"). Funding from MES RK state-targeted program BR05236454 is also acknowledged.

[1] O. Matoba, T. Nomura, E. Perez-Cabre, M. S. Millan, and B. Javidi, Optical techniques for information security, Proc. IEEE **97**, 1128 (2009).

[2] 2018 U.S. Department of Defense MURI Awards, Non-Equilibrium Dynamics: Magnet-Free Non-Reciprocal Metamaterials Based on Spatio-Temporal Modulation, PI: Andrea

Alu, http://media.defense.gov/2018/Apr/02/2001898337/-1/-1/1/MURI-2018-AWARDS-ANNOUNCEMENT.PDF, April 2018.

[3] J. K. Gansel, M. Thiel, M. S. Rill, M. Decker, K. Bade, V. Saile, G. von Freymann, S. Linden, and M. Wegener, Gold helix photonic metamaterial as broadband circular polarizer, Science, **325**, 1513 (2009).

[4] C. Menzel, C. Helgert, C. Rockstuhl, E.-B. Kley, A. Tunnermann, T. Pertsch, and F. Lederer, Asymmetric Transmission of Linearly Polarized Light at Optical Metamaterials, Phys. Rev. Lett. **104**, 253902 (2010).

[5] J. Lin, J. P. B. Mueller, Q. Wang, G. Yuan, N. Antoniou, X. Yuan, and F. Capasso, Polarization-controlled tunable directional coupling of surface plasmon polaritons, Science **340**, 331 (2013).

[6] N. Engheta, Circuits with light at nanoscales: Optical nanocircuits inspired by metamaterials, Science **317**, 1698 (2007).

[7] T. Niemi, A. O. Karilainen, and S. A. Tretyakov, Synthesis of polarization transformers, IEEE Trans. Antennas Propag. **61**, 3102 (2013).

[8] Z. Wei, Y. Cao, Y. Fan, X. Yu, and H. Li, Broadband polarization transformation via enhanced asymmetric transmission through arrays of twisted complementary split-ring resonators, Appl. Phys. Lett. **99**, 221907 (2011).

[9] A. Arbabi, Y. Horie, M. Bagheri, and A. Faraon, Dielectric metasurfaces for complete control of phase and polarization with subwavelength spatial resolution and high transmission, Nat. Nanotechnol. **10**, 937 (2015).

[10] N. K. Grady, J. E. Heyes, D. R. Chowdhury, Y. Zeng, M. T. Reiten, A. K. Azad, A. J. Taylor, D. A. R. Dalvit, and H. Chen, Terahertz metamaterials for linear polarization conversion and anomalous refraction, Science **340**, 1304 (2013).

[11] M. Borgese, F. Costa, S. Genovesi, A. Monorchio, and G. Manara, Optimal design of miniaturized reflecting metasurfaces for ultra-wideband and angularly stable polarization conversion, Sci. Rep. **8**, 7651 (2018).

[12] C. Pfeiffer, C. Zhang, V. Ray, L. J. Guo, and A. Grbic, Polarization rotation with ultra-thin bianisotropic metasurfaces, Optica **3**, 427 (2016).

[13] Y. Zhao, M. A. Belkin, and A. Alu, Twisted optical metamaterials for planarized ultrathin broadband circular polarizers, Nat. Commun. **3**, 870 (2012).

[14] I. Crassee, J. Levallois, A. L. Walter, M. Ostler, A. Bostwick, E. Rotenberg, T. Seyller, D. Marel, and A. B. Kuzmenko, Giant Faraday rotation in single- and multilayer graphene, Nat. Phys. **7**, 48 (2011).

[15] C. A. Valagiannopoulos, M. Mattheakis, S. N. Shirodkar, and E. Kaxiras, Manipulating polarized light with a planar slab of black phosphorus, J. Phys. Com. **1**, 045003 (2017).

[16] R. Alaee, J. Christensen, and M. Kadic, Optical Pulling and Pushing Forces in Bilayer $\mathscr{P}\mathscr{T}$-Symmetric Structures, Phys. Rev. Appl. **9**, 014007 (2018).

[17] A. N. Papadimopoulos, N. V. Kantartzis, N. L. Tsitsas, and C. A. Valagiannopoulos, Wide-angle absorption of visible light from simple bilayers, Appl. Opt. **56**, 9779 (2017).

[18] S. Savoia, G. Castaldi, V. Galdi, A. Alù, and N. Engheta, Tunneling of obliquely incident waves through $\mathscr{P}\mathscr{T}$-symmetric epsilon-near-zero bilayers, Phys. Rev. B **89**, 085105 (2014).

[19] M. D. Johnson, C. Orme, A. W. Hunt, D. Graff, J. Sudijono, L. M. Sander, and B. G. Orr, Stable and Unstable Growth in Molecular Beam Epitaxy, Phys. Rev. Lett. **72**, 116 (1994).

[20] R. W. Johnson, A. Hultqvist, and S. F. Bent, A brief review of atomic layer deposition: From fundamentals to applications, Mater. Today **17**, 236 (2016).

[21] B. D. Gates, Q. Xu, M. Stewart, D. Ryan, C. G. Willson, and G. M. Whitesides, New approaches to nanofabrication: Molding, printing, and other techniques, Chem. Rev. **105**, 1171, (2005).

[22] D. A. Pawlak, S. Turczynski, M. Gajc, K. Kolodziejak, R. Diduszko, K. Rozniatowski, J. Smalc, and I. Vendik, How far are we from making metamaterials by self-organization? The microstructure of highly anisotropic particles with an SRR-Like geometry, Adv. Funct. Mater. **20**, 1116 (2010).

[23] A. H. Sihvola, *Electromagnetic Mixing Formulas and Applications*, IEE electromagnetic waves series, Vol. 47 (IEE Press, London, 1999).

[24] A. Agarwal, M. S. Vitiello, L. Viti, A. Cupolillo, and A. Politano, Plasmonics with two-dimensional semiconductors: From basic research to technological applications, Nanoscale **10**, 8938 (2018).

[25] M. Mattheakis, C. A. Valagiannopoulos, and E. Kaxiras, Epsilon-near-zero behavior from plasmonic Dirac point: Theory and realization using two-dimensional materials, Phys. Rev. B **94**, 201404 (2016).

[26] K. Majhi, B. S. Prakash, and K. B. R. Varma, Extreme values of relative permittivity and dielectric relaxation in Sr_2SbMnO_6 ceramics, J. Phys. D **40**, 7128 (2007).

[27] I. Liberal and N. Engheta, Near-zero refractive index photonics, Nat. Phot. **11**, 149 (2017).

[28] M. Scalora, G. D'Aguanno, N. Mattiucci, M. J. Bloemer, D. de Ceglia, M. Centini, A. Mandatori, C. Sibilia, N. Akozbek, M. G. Cappeddu, M. Fowler, and J. W. Haus, Negative refraction and sub-wavelength focusing in the visible range using transparent metallodielectric stacks, Opt. Express **15**, 508 (2007).

[29] J. Sun, J. Zeng, and N. M. Litchinitser, Twisting light with hyperbolic metamaterials, Opt. Express **21**, 14975 (2013).

[30] L. Ge, Y. Cang, K. Gong, L. Zhou, D. Yu, and Y. Luo, Manipulating polarization of light with ultrathin epsilon-near-zero metamaterials, Opt. Express **21**, 11441 (2013).

[31] I. Fedorin, Polarization transformation by a hyperbolic metamaterial on a metal substrate, Prog. Electromagn. Res. B **67**, 17 (2016).

[32] O. V. Kotov and Y. E. Lozovik, Enhanced optical activity in hyperbolic metasurfaces, Phys. Rev. B **96**, 235403 (2017).

[33] H. Zhu, X. Yin, L. Chen, Z. Zhu, and X. Li, Manipulating light polarizations with a hyperbolic metamaterial waveguide, Opt. Lett. **40**, 4595 (2015).

[34] M. Fruhnert, A. Monti, I. Fernandez-Corbaton, A. Alù, A. Toscano, F. Bilotti, and C. Rockstuhl, Tunable scattering cancellation cloak with plasmonic ellipsoids in the visible, Phys. Rev. B **93**, 245127 (2016).

[35] http://refractiveindex.info/ (accessed August 11 2018).

[36] K. M. McPeak, S. V. Jayanti, S. J. P. Kress, S. Meyer, S. Iotti, A. Rossinelli, and D. J. Norris, Plasmonic films can easily be better: Rules and recipes, ACS Photonics **2**, 326 (2015).

[37] C. A. Valagiannopoulos, Optical $\mathscr{P}\mathscr{T}$-symmetric counterparts of ordinary metals, IEEE J. Sel. Top. Quantum Electron. **22**, 89 (2016).

[38] G. V. Naik, V. M. Shalaev, and A. Boltasseva, Alternative plasmonic materials: Beyond gold and silver, Adv. Mater. **25**, 3264 (2013).

[39] G. W. Hanson, Dyadic Green's functions and guided surface waves for a surface conductivity model of graphene, J. Appl. Phys. **103**, 064302 (2008).

[40] D. Rodrigo, T. Low, D. B. Farmer, H. Altug, and P. Avouris, Plasmon coupling in extended structures: Graphene superlattice nanoribbon arrays, Phys. Rev. B **93**, 125407 (2016).

[41] T. Guo and C. Argyropoulos, Broadband polarizers based on graphene metasurfaces, Opt. Lett. **41**, 5592 (2016).

[42] T. E. Tiwald, J. A. Woollam, S. Zollner, J. Christiansen, R. B. Gregory, T. Wetteroth, S. R. Wilson, and A. R. Powell, Carrier concentration and lattice absorption in bulk and epitaxial silicon carbide determined using infrared ellipsometry, Phys. Rev. B **60**, 11464 (1999).

[43] E. Shkondin, Fabrication of hyperbolic metamaterials using atomic layer deposition, Ph.D. thesis, supervisors: A. Lavrinenko and F. Jensen, Technical University of Denmark, 2016.

[44] M. Prasciolu and S. Bajt, On the properties of WC/SiC multilayers, Appl. Sci. **8**, 571 (2018).

[45] E. A. Filatova, D. Hausmann, and S. D. Elliott, Investigating routes toward atomic layer deposition of silicon carbide: Ab initio screening of potential silicon and carbon precursors, J. Vac. Sci. Technol. A **35**, 01B103 (2016).

[46] A. Fissel, B. Schröter, and W. Richter, Low-temperature growth of SiC thin films on Si and 6H-SiC by solid-source molecular beam epitaxy, Appl. Phys. Lett. **66**, 3182 (1995).

[47] V.-C. Su, C. H. Chu, G. Sun, and D. P. Tsai, Advances in optical metasurfaces: Fabrication and applications, Opt. Express **26**, 13148 (2018).

[48] W. Luo, S. Sun, H.-X. Xu, Q. He, and L. Zhou, Transmissive Ultrathin Pancharatnam-Berry Metasurfaces with nearly 100% Efficiency, Phys. Rev. Appl. **7**, 044033 (2017).

[49] M. Gonidec, M. M. Hamedi, A. Nemiroski, L. M. Rubio, C. Torres, and G. M. Whitesides, Fabrication of nonperiodic metasurfaces by microlens projection lithography, Nano Lett. **16**, 4125 (2016).

[50] A. D. Boardman, P. Egan, and M. McCall, Optic axis-driven new horizons for hyperbolic metamaterials, EPJ Appl. Metamat. **2**, 11 (2015).

[51] R. C. Devlin, A. Ambrosio, N. A. Rubin, J. P. Balthasar Mueller, and F. Capasso, Arbitrary spin-to-orbital angular momentum conversion of light, Science **358**, 896 (2017).

[52] A. E. Willner, H. Huang, Y. Yan, Y. Ren, N. Ahmed, G. Xie, C. Bao, L. Li, Y. Cao, Z. Zhao, and J. Wang, Optical communications using orbital angular momentum beams, Adv. Opt. Photonics **7**, 66 (2015).